THE ASTROPHYSICAL JOURNAL, 379:271–279, 1991 September 20

THE MOLECULAR ENVELOPE OF NGC 7027

JOHN H. BIEGING,[1,2] DAVID WILNER,[1] AND HARLEY A. THRONSON, JR.[3]

Received 1991 January 11; accepted 1991 April 3

ABSTRACT

We present maps of the $J = 1$–0 emission line of CO toward the planetary nebula NGC 7027. The images were made by combining interferometer observations from the Berkeley-Illinois-Maryland Array (BIMA) with single-dish observations from the NRAO 12 m telescope. The maps have an angular resolution of 5″ and contain all the flux in the CO $J = 1$–0 line. The integrated intensity map shows that the circumstellar molecular envelope has a diameter to zero intensity of ~70″, corresponding to a linear size of 0.30 pc at distance of 900 pc. The envelope has an axisymmetric, clumpy appearance, with unresolved clumps having a size of <0.02 pc. Maps at the line center reveal a bright inner ring of CO emission which surrounds a central CO minimum coincident with the ionized gas. The neutral envelope possesses axial symmetry which is aligned with the symmetry axis of the ionized nebula. The expansion of the molecular gas is evident in position-velocity maps, especially along the symmetry axis (P.A. 150°), and in the orthogonal direction. The morphology of the CO emission implies that (1) the molecular material is constraining the development of the ionized nebula; (2) mass loss from the central star was neither spherically symmetric nor completely uniform in time; and (3) the molecular envelope contains significant structure on scales smaller than 5″.

Subject headings: nebulae: individual (NGC 7027) — nebulae: planetary — stars: circumstellar shells

1. INTRODUCTION

Planetary nebulae are the ionized, fluorescing remnants of circumstellar matter ejected from evolved stars. The last stages of giant-branch evolution are characterized by copious mass loss, which produces a cool, molecular circumstellar shell (see, e.g., Menessier & Omont 1990). When mass loss removes the outer layers of the star, the remnant hot core is revealed as a white dwarf with a temperature sufficiently high to photoionize the surrounding envelope. From this evolutionary picture one expects that very young planetary nebulae will still be surrounded by a neutral molecular shell, while old nebulae should show little or no remnant neutral gas.

Such remnant molecular gas has now been found toward 19 planetary nebulae by Huggins & Healy (1989), whose results confirm the evolutionary connection between molecular circumstellar envelopes and planetary nebulae. A few young planetary nebulae have been mapped in the CO $J = 1$–0, 2–1, or 3–2 transitions, including IRAS 21282 + 5050 (Shibata et al. 1989), NGC 2346 (Healy & Huggins 1988; Bachiller et al. 1989b), NGC 6720 (the Ring Nebula; Bachiller et al. 1989a), and NGC 7027 (Mufson, Lyon, & Marionni 1975; Masson et al. 1985; Phillips, White, & Richardson 1985; Thronson & Bally 1986; Deguchi et al. 1990; Jaminet et al. 1991). In general, resolved images of the CO emission are consistent with the idea that the molecular envelope surrounds the ionized nebula.

NGC 7027 was the first planetary nebula to be detected in CO emission, by Mufson et al. (1975), who mapped the source and concluded that the molecular envelope was some 5 times the size of the optical nebula and had a mass which was several times that of the ionized gas. Subsequent CO observations of NGC 7027 improved on the quality of the spectra (Thronson 1983; Knapp & Morris 1985) but not on the angular resolution. Recently, Deguchi et al. (1990) have obtained CO spectra with 18″ resolution for a five-point cross and find evidence for asymmetries in the brightness distribution, but they do not present a fully sampled map of the extended CO nebula. Pioneering work by Masson et al. (1985) with the Owens Valley millimeter-wavelength interferometer produced images of NGC 7027 in the CO $J = 1$–0 line with an angular resolution of ~7″ × 10″, which resolved the molecular envelope and showed a flattened gas distribution which Masson et al. modeled as an oblate spheroid whose major axis was orthogonal to the major axis of the ionized gas as projected on the sky. They concluded that the density distribution of the neutral gas was constraining the growth of the H II region in the equatorial plane. The total envelope mass was found to be ~1.5 $M_\odot$, adopting a distance of 0.9 kpc (Masson 1989; note that this distance has an uncertainty of 17%, so all linear dimensions based on this distance have a corresponding uncertainty.)

The results of Masson et al. (1985) suffered from a lack of low spatial frequency data (i.e., short interferometer baselines), so that ~90% of the CO flux density was missing in their maps of the central velocity channels. Since to first order the envelope is expected to be expanding uniformly, the central velocity should show the envelope in cross section and so give the most unambiguous measure of the structure of the neutral envelope, free of projection effects. This shortcoming of the Masson et al. (1985) results led us to undertake to map the CO emission toward NGC 7027 using a combination of single-dish and interferometry data. The single-dish observations were made with the NRAO[4] 12 m telescope at Kitt Peak, Arizona, and the interferometer observations were made with the three-element Berkeley-Illinois-Maryland Array (BIMA) at Hat Creek, California. By combining the data sets appropriately,

[1] Radio Astronomy Laboratory, University of California, Berkeley, CA 94720.
[2] Steward Observatory, University of Arizona, Tucson, AZ 85721.
[3] Wyoming Infrared Observatory, Box 3905, University of Wyoming, Laramie, WY 82070.

[4] The National Radio Astronomy Observatory is operated by Associated Universities, Inc., under a cooperative agreement with the National Science Foundation.

we obtained images with 5″ spatial resolution, 0.8 km s^{-1} velocity resolution, and no missing flux. The images presented in this paper should therefore give the most complete picture to date of the neutral circumstellar cloud within which the planetary nebula NGC 7027 is evolving.

2. OBSERVATIONS AND DATA REDUCTION

2.1. *Single-Dish Observations*

NGC 7027 was mapped in the $J = 1$–0 rotational line of CO at 115.271 GHz with the NRAO 12 m telescope. The source was observed on a 9 × 11 rectangular grid of points spaced 20″ apart. The region mapped was sufficient to cover all of the detectable CO emission. The telescope beamwidth at 115 GHz is predicted to be 54″ (HPBW) based on a measurement on Jupiter at 96.75 GHz (P. Jewell, private communication), with an estimated uncertainty of ±2″. A contour map of the CO line intensity averaged over the velocity range 10–40 km s^{-1} is shown in Figure 1. Small distortions of the contours reflect calibration or pointing errors in the individual spectra and in groups of spectra along single rows of the grid.

Observations were made by standard position switching. Typical system temperatures were 1200 K (SSB) referred to outside the atmosphere for a lossless antenna. Calibration was by the standard chopper wheel method (Ulich & Haas 1976; Kutner & Ulich 1981). The spectrometer consisted of parallel filter banks of 128 250 kHz filters for each of the two orthogonal circular polarizations received. The velocity coverage was therefore 83 km s^{-1}, with a channel separation of 0.65 km s^{-1}. The on-source integration time per grid point was 180 s, which yielded a typical rms noise level after averaging polarizations of 0.24 K for each spectrum. After every 10 observations of the map grid, the central position was observed as a check on the pointing and calibration. Figure 2 shows the averaged spectrum for the central position. The spectrum is in good agreement with previous work (e.g., Thronson 1983; Knapp & Morris 1985; Deguchi et al. 1990). The apparent absorption dip at +5 km s^{-1} may be a result of weak emission in the reference position. (Note that at the position of NGC 7027, local interstellar gas is expected to have LSR velocities near 0 km s^{-1}.) The parabolic line shape of Figure 2 is expected for partially resolved optically thick emission from a spherically symmetric expanding source (e.g., Morris 1975). The flux density scale of the spectrum assumes an efficiency factor of 39 Jy K^{-1} (T_A^*) for the 12 m telescope at 115 GHz (P. Jewell, private communication).

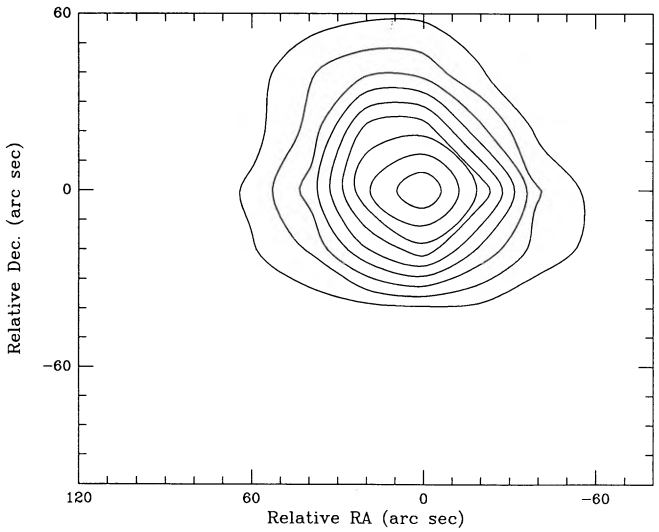

FIG. 1.—Contour map of CO $J = 1$–0 brightness, averaged over the veocity range 10–40 km s^{-1}, from the NRAO 12 m single-dish data only. The maximum intensity is 148 Jy and the contour interval is 14.8 Jy. The grid origin is at 21^{h}05^{m}09^s.4, 42°02′03″ (equinox 1950.0). The entire region shown was sampled at 20″ spacings on a 9 × 11 grid.

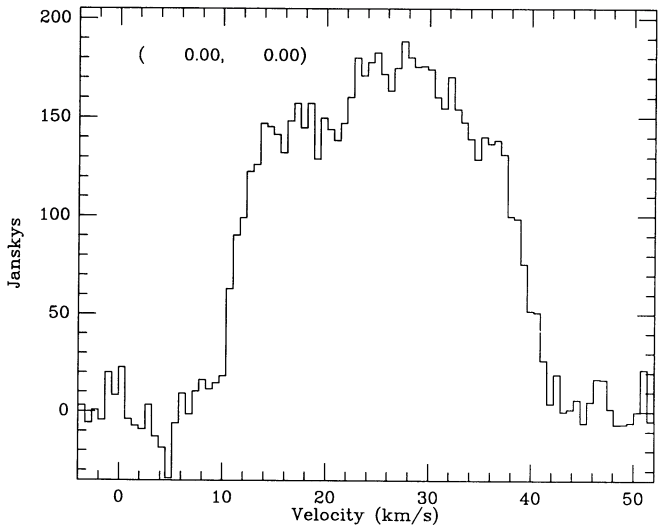

FIG. 2.—CO $J = 1$–0 spectrum from the NRAO 12 m single-dish data, for the (0, 0) grid position. Abscissa is LSR velocity.

2.2. *Interferometer Observations*

NGC 7027 was observed with the three-element BIMA interferometer in each of five antenna configurations for a total of 15 independent baselines. The maximum projected antenna spacings were 30 kilowavelengths north-south and 36 kilowavelengths east-west. The points sampled in the Fourier-transform (u, v)-plane are shown in Figure 3.

The interferometer observations were made by cycling between the souce and a phase and amplitude calibrator. The phase tracking center for NGC 7027 was R.A. = 21^{h}05^{m}09^s.4, Decl. = +42°02′03″.0 (equinox 1950.0). The phase and amplitude calibrators were 3C 345 and 3C 454.3. Source observations were 30 minutes long, bracketed by 9 minutes calibrator observations. The instrumental phase and gain were determined with the standard BIMA reduction software (RALINT). The calibrator flux densities were determined by comparison with planets, or with 3C 84 or 3C 273, which were in turn calibrated against the planets. The planetary flux densities were determined by adopting the brightness temperature scale of Ulich (1981) and calculating the visibility of the planet for each interferometer baseline. The estimated accuracy of the amplitude calibration is ±20%.

The interformeter observations employed a 512 channel digital cross-correlation spectrometer (Urry, Thornton, & Hudson 1985). The CO line was observed with 128 channels of 20 MHz total bandwidth, giving a separation of 156.25 kHz or 0.41 km s^{-1}. The effective velocity resolution was a factor of 1.2 larger, or 0.49 km s^{-1}. The spectrometer bandpass was calibrated by 40 minute observations of 3C 84, 3C 273, or a planet (on the shorter baselines).

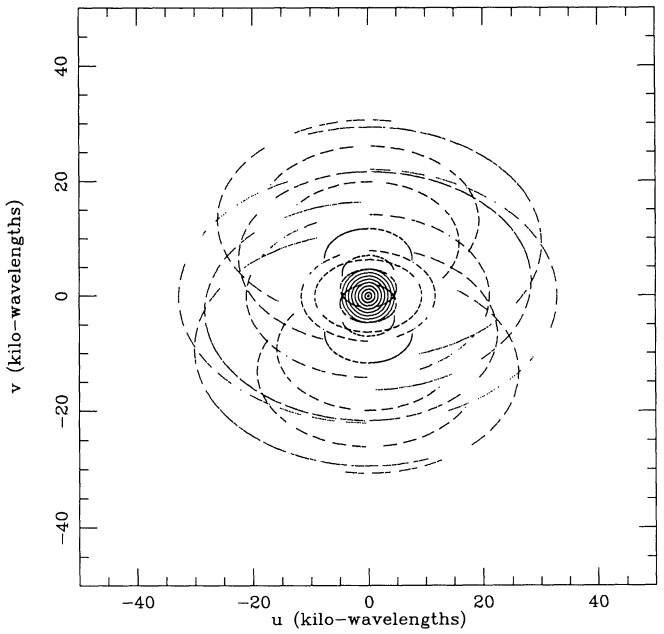

FIG. 3.—Location of points in the (u, v)-plane sampled by the BIMA interferometer and extracted from the NRAO single-dish maps. The small concentric circles close to the origin show the loci of visibility points calculated by Fourier-transforming the single-dish data. The weighting scheme used in constructing the maps is described in the text.

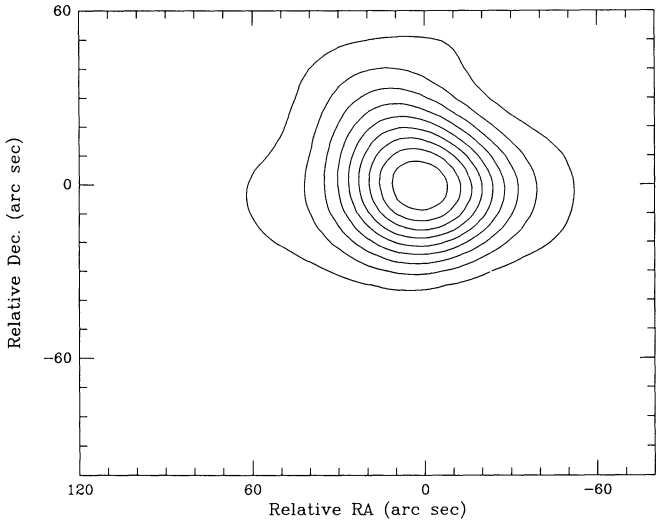

FIG. 4.—The single-dish map of Fig. 1 after Fourier transforming to the visibility domain and then transforming back. Note how the small-scale features of Fig. 1 (attributable to calibration and/or pointing errors) have been filtered out by the Fourier transform process. The peak intensity is 145 Jy, and the contour interval is 10%.

2.3. *Combining Single-Dish and Interferometer Data*

As noted in the Introduction, previous inteferometer observations of the CO $J = 1$–0 line toward NGC 7027 (Masson et al. 1985) suffered from a lack of information at short baselines, because the emission is extended on a scale of at least 40″ (see Mufson, Lyon, & Marionni 1975 and Fig. 1) and so has significant correlated flux at low spatial frequencies. In the present work, we obtained the low spatial frequency information by mapping the source with the NRAO 12 m telescope. The single-dish maps contain information on spatial frequencies extending (with decreasing weight) from 0 to the inverse of the primary beamwidth (54″) or to ~4600 wavelengths in the (u, v)-plane. By combining this spatial information with that obtainend by the interferometer, we can construct images which include all the CO line flux density and which accurately represent the source structure down to the resolution of the longest interferometer baselines.

The method of combining the two data sets was similar to that described by Vogel et al. (1984) and Weliachew et al. (1985). The single-dish maps were Fourier-transformed to a set of eight simulated interferometer baselines which consisted of circular tracks in the (u, v)-plane with radii of 5, 10, ..., 40 light-ns (10 light-ns = 1150 wavelengths at the observing frequency). These circular tracks are shown in Figure 3, where they fill the region near the origin.

The single-dish map of Figure 1 is the true source brightness distribution convolved with the 12 m telescope beam and multiplied by some function representing calibration errors. To sufficient accuracy, the 12 m beam can be considered a Gaussian with 54″ HPBW. Since we wish to combine the 12 m single-dish data with the interferometer data, we first remove the effect of this convolution by dividing the simulated visibility data (on the eight circular tracks) by the Fourier transform of the 54″ HPBW Gaussian. Next, because the single-dish data must be combined with BIMA interferometer data obtained with 6 m antennas each having a 106″ HPBW, we convolve the simulated single-dish visibilities with the Fourier transform of a 106″ Gaussian. By the convolution theorem, this operation is equivalent to multiplying the brightness distribution in the (x, y) plane of the sky by the primary response of the 6 m interferometer antennas.

After these operations, the simulated visibilities for the 8 circular tracks were transformed back to the (x, y)-plane to check that the resulting image is a faithful representation of the original single-dish image. Figure 4 shows such an image, made by averaging over the velocity range 10–40 km s^{-1} (LSR), i.e., the same range as in Figure 1. The (simulated) (u, v) data were weighted with a Gaussian taper which fell to 50% at 1750 wavelengths. This weighting produced a circular, nearly Gaussian beam with a half-power diameter of 56″, which closely matches the measured size of the 12 m telescope beam. Note, in comparing Figure 4 with the original single-dish map in Figure 1, that the images are very similar except that Figure 4 lacks the small-scale distortions seen in the contours of Figure 1. This smoother apearance is a result of the Fourier transform process which has filtered out the high-spatial frequency "information" (actually small-scale calibration or pointing errors). Note also that the peak brightness temperatures of the two maps are nearly identical, which confirms that the weighting scheme (1750 wavelength taper) and resultant beam size accurately match the 12 m telescope beam. In short, Figure 4 shows that our method of obtaining the low-spatial-frequency information in the visibility domain does accurately represent the single-dish data. We made this same comparison for a set of images covering the velocity range 0–40 km s^{-1} with widths of 5 km s^{-1}. In each case, the simulated interferometer maps matched the original single-dish maps in peak intensity and overall morphology.

NGC 7027 has a continuum flux density of ~4.8 Jy at 115 GHz (see Masson et al. 1985). The 12 m spectra are insensitive

to the continuum, since a linear baseline has been removed. We therefore added a point source of 4.8 Jy to the short-spacing visibilities derived from the single-dish data, since the continuum source is unresolved in the 12 m telescope beam. The interferometer data, of course, do contain the continuum visibility as well as the CO line.

The BIMA interferometer visibility data were treated in the standard way. The data were weighted in inverse proportion to the square of the effective system temperature for each data point. No taper was applied to the visibilities. When the interferometer data alone were transformed to images by the usual gridding and Fourier transform, the resulting "dirty" beam had a full width at half-maximum of 5".7 × 4".7. As a check we used only the BIMA interferometer data suitably weighted to make maps with the same angular resolution and velocity sampling as the results of Masson et al. (1985). The resulting maps agreed well with those of Masson et al.

The single-dish and interferometer visibility spectra were smoothed in velocity and rebinned at integer values of LSR velocity, so that the velocity sampling of the two data sets was identical. The two visibility data sets were convolved onto identical square grids in the (u, v)-plane and two sets of gridded weights were constructed according to the schemes described above. The gridded visibilities and weights were then added together with normalized scale factors which were in inverse proportion to the synthesized beam areas, i.e., $1/(56'')^2$ for the single dish data and $1/(5''.7 \times 4''.7)$ for the interferometer data. Since the visibility data are in Janskys, this weighting is necessary to obtain the proper brightness temperature scale for the combined map.

The gridded, combined visibility data were Fourier transformed to images. The resulting "dirty" beam had a size of 5".7 × 4".7 (HPBW), as expected from the maximum baselines in the interferometer data. Note, however, that because the (u, v) sampling (Fig. 3) covers the innermost part of the visibility plane well, the resulting images contain the flux density measured by the single-dish maps.

The resulting maps were cleaned with the standard algorithm in the RALINT software, with a 5".7 × 4".7 (HPBW) Gaussian restoring beam and a loop gain of 0.1. Typically, ~1000 iterations were required for velocity channels in the center of the CO emission line, while less than 100 iterations were needed at the extreme velocities.

3. RESULTS

Cleaned images from the combined data sets are shown in Figure 5, for 16 velocity intervals each 2 km s^{-1} wide centered at 11, 13, ..., 41 km s^{-1} (LSR). This velocity range covers all the CO emission detected in the single-dish spectrum (see Fig.

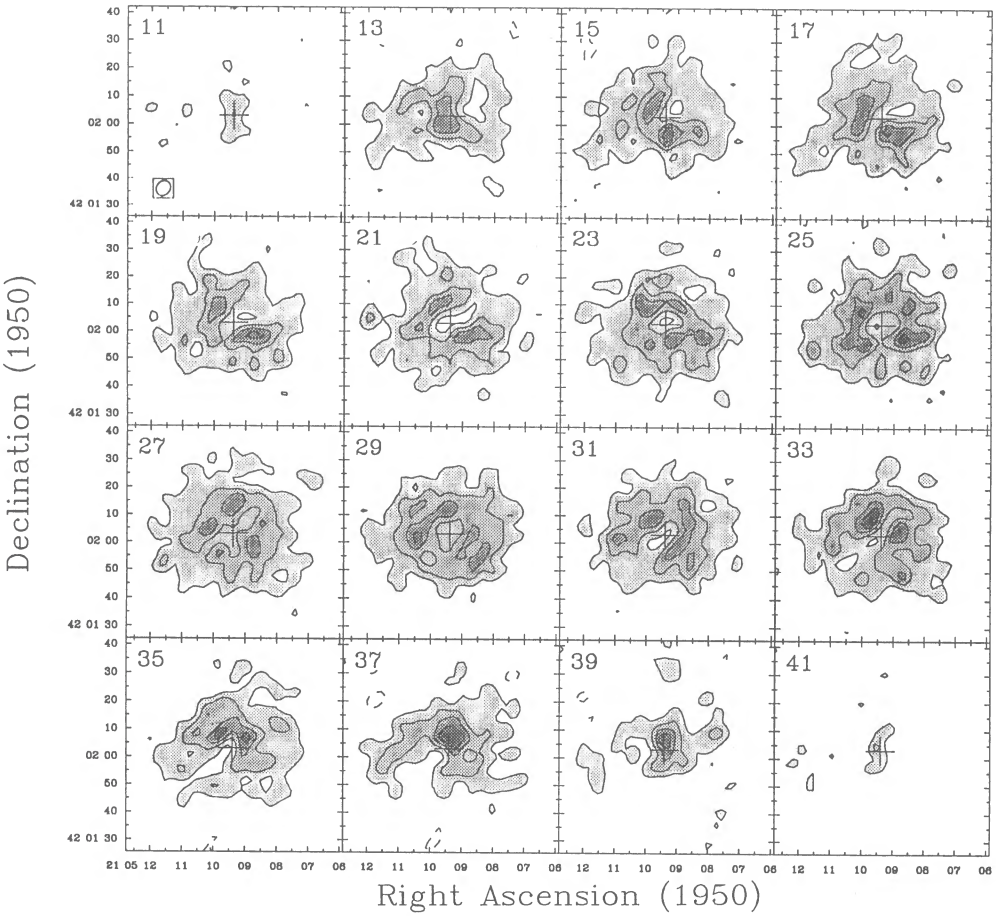

FIG. 5.—Montage of brightness distribution maps derived from the combined single-dish and interferometer data. Each map covers a 2 km s^{-1} wide velocity channel. Center velocity is given in the upper left of each map. Contour interval is 1.5 Jy per clean beam area, corresponding to ~4 times the rms noise level. The central continuum source has been subtracted from these maps. The HPBW of the synthesized clean beam (5".7 × 4".8) is shown in the corner of the top left image.

2). The contour interval is 1.2 Jy per clean beam area, or 4.0 K in brightness temperature. This contour unit is ~3 times the rms noise level of the cleaned maps, which was typically 1.3 K for a velocity width of 2 km s^{-1}. These maps have had an average continuum map subtracted, to remove the (small) effect of the free-free emission from the ionized gas, which has a total flux density of ~4.8 Jy at 115 GHz (cf. Masson et al. 1985). The continuum map was made by averaging all off-line channels. The images of Figure 5 show that at the extreme velocities (11 and 41 km s^{-1}) the CO emission peaks up at the central position, toward the central star. At intermediate velocities, the CO is extended and shows a ringlike distribution with a local minimum toward the star. The CO emission has a bifurcated appearance in velocities from 17 to 33 km s^{-1}. There is a rather well-defined symmetry axis at P.A. ~150°. At 13 km s^{-1}, the peak CO intensity lies ~5″ SE of the center. At 15 km s^{-1} the emission begins to split into two parts which curve up and around the center. From 17 to 33 km s^{-1}, there are two distinct CO maxima which lie nearly symmetrically about a line through the center at P.A. 150°. As the velocity increases, the two peaks shift up to the NW, moving around the center. At 35–37 km s^{-1}, the peaks have joined together ~5″ NW of the center position. The variation of CO morphology and size with velocity implies that the molecular envelope around NGC 7027 is expanding radially, with axial (but not spherical) symmetry. The symmetry axis, projected on the plane of the sky, has the same position angle as the symmetry axis of the ionized gas (see Masson 1986, 1989).

The spectrum for the central position, shown in Figure 6, has two sharp horns at the extreme velocities, as expected for a well-resolved expanding shell. Position-velocity diagrams for cuts at P.A. 60° and 150° are shown in Figures 7 and 8. These images show a bright ring of emission with an elliptical shape, which is consistent with an expanding (hollow) shell of emitting gas. The figures show asymmetries which, like the images of Figure 5, are inconsistent with spherically symmetric expansion. Note how the brightest peaks are displaced from the central position (the origin on the vertical axis), to the negative side at 13 km s^{-1} and the positive side at 38 km s^{-1}, and the peaks individually show an asymmetry about the reference position. To show in more detail the full extent of the molecular envelope around the planetary nebula, Figure 9 is a contour map of the CO emission integrated in velocity between 23 and 27 km s^{-1}. This velocity range is centered at the central velocity of the CO line and is narrow compared to the total line width. If the gas is expanding radially with approximately

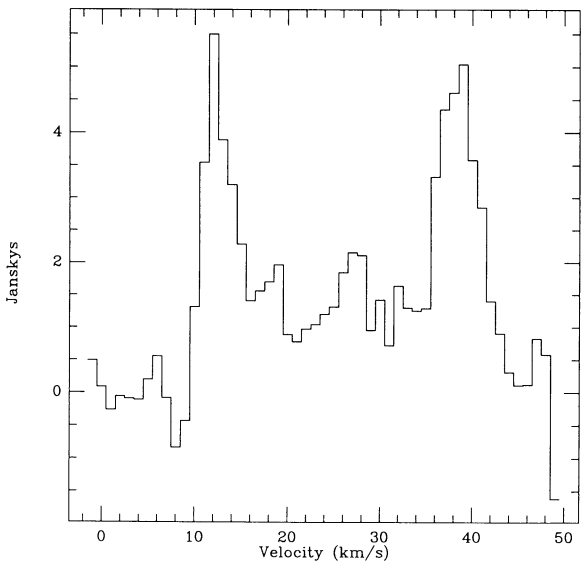

FIG. 6.—Spectrum of CO $J = 1$–0 line for the central position of the combined single-dish and interferometer maps. The velocity resolution here is 1 km s^{-1}.

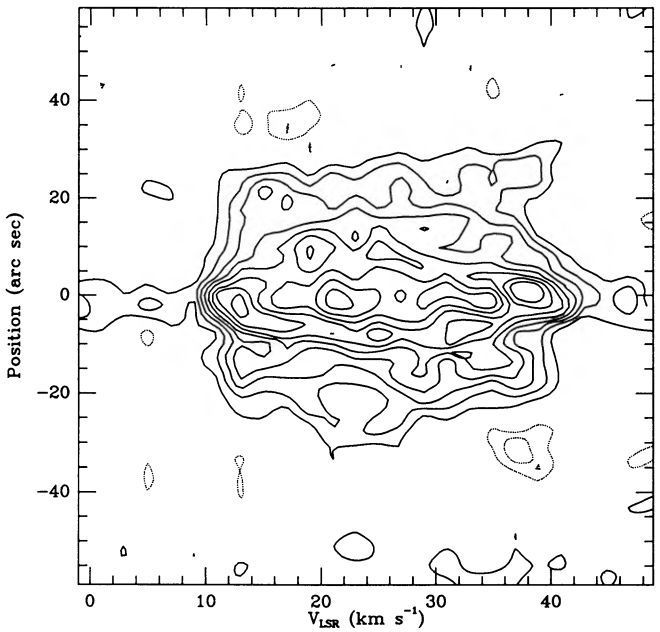

FIG. 7.—Position-velocity contour map for an axis through the central position at P.A. 60° (orthogonal to the symmetry axis—see text). Contour interval is 0.66 Jy per clean beam; velocity resolution is 2 km s^{-1}.

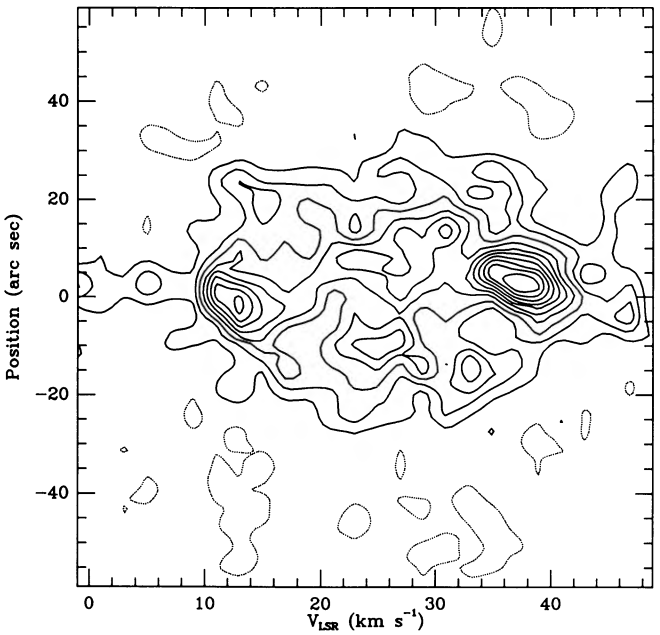

FIG. 8.—As for Fig. 7, at P.A. 150° (along the symmetry axis)

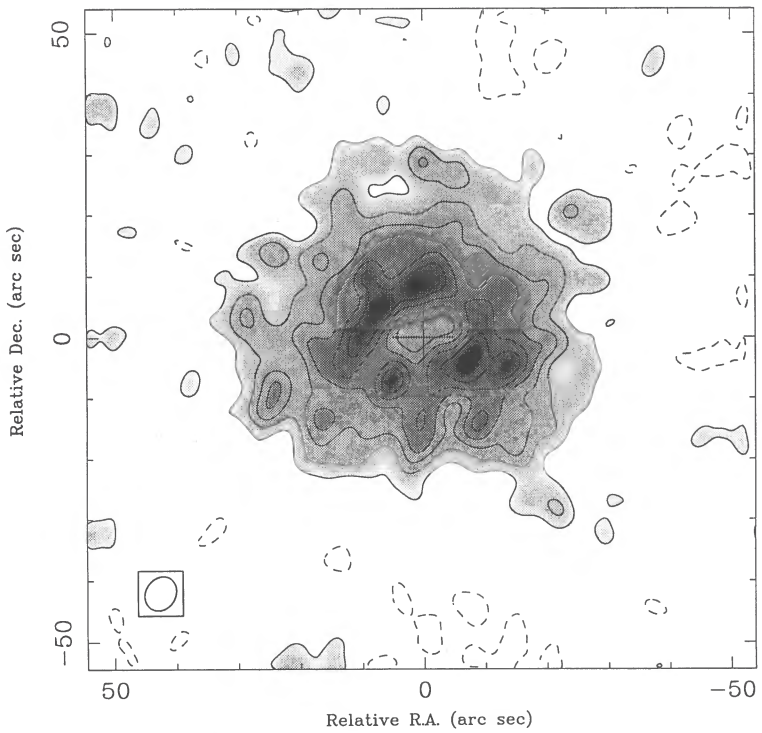

FIG. 9.—Gray scale and contour map of combined single-dish and interferometer data for velocity interval 23–27 km s^{-1} (LSR), i.e., centered on the systemic velocity. This image approximates a cross section through the radially expanding envelope. Contour interval is 2.0 K T_B (=0.60 Jy per clean beam).

spherical symmetry, then Figure 9 represents a cross section through the envelope in the plane of the sky. There is a central minimum in the CO emission which coincides with the location of the ionized gas. Surrounding this minimum is a bright ring of CO emission which is not completely uniform but has three or four gaps—areas of reduced intensity. Beyond the bright inner ring the CO emission extends to a diameter of ~70″.

Although the CO in this velocity range has a roughly circular appearance, there are a number of bright clumps within the extended emission. These clumps have intensities well above the rms noise level, and most are visible in more than one velocity channel in Figure 5. We therefore believe that these features are real enhancements in either the CO excitation temperature or optical depth. Since, as will be discussed below, the CO $J = 1$–0 emission is probably not optically thick through most of the envelope seen in Figure 9, these bright clumps are probably regions of enhanced CO $J = 1$–0 optical depth.

Despite the somewhat clumpy appearance of Figure 9, it is useful to examine the average radial profile of the brightness distribution. Figure 10 shows the CO brightness temperature of Figure 9 averaged around circles, as a function of radius from the center. Figure 10 clearly shows the central minimum and the surrounding bright ring. The maximum average brightness temperature of the ring is ~12 K at a radius of 9″. Beyond that, the brightness temperature falls smoothly to zero at a radius of ~35″ ± 5″.

4. DISCUSSION

4.1. *CO Optical Depth and Excitation Temperature*

The interpretation of these CO images depends critically on the optical depth and excitation temperature of the $J = 1$–0 transition. We cannot determine the optical depth of the line with the $J = 1$–0 data alone. However, observations of the CO $J = 3$–2 line at 345 GHz have been obtained by Jaminet et al. (1991), who have performed a statistical equilibrium calculation for a simple model molecular envelope. Jaminet et al. use both the $J = 3$–2 observations (with 14″ HPBW resolution) and the $J = 1$–0 data presented in this paper, but smoothed to 14″ resolution, to constrain their model. The most important conclusion of that study for interpreting our $J = 1$–0 data is that the $J = 1$–0 line is *not* very optically thick. Specifically, Jaminet et al. find that, to fit the observed spectra of the

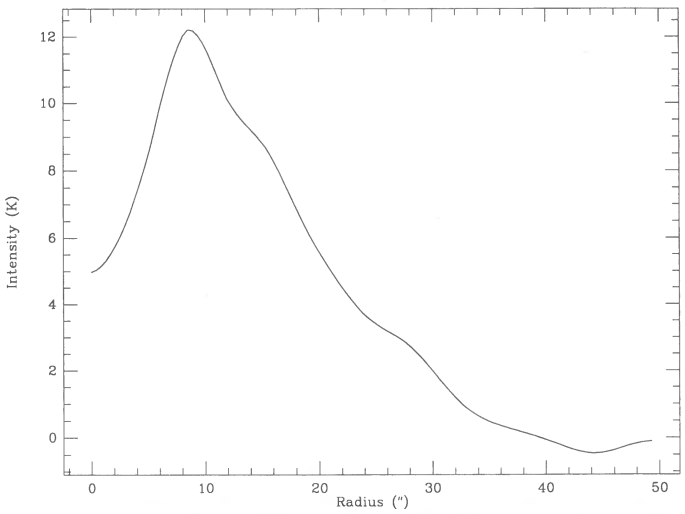

FIG. 10.—Radial profile of CO emission in Fig. 9. Ordinate is the brightness (in K) averaged around a circle of given radius, centered on the map origin.

$J = 1$–0 and 3–2 lines, the average $J = 1$–0 optical depth is close to unity. A similar conclusion—that $\tau(J = 1\text{–}0) \approx 1$—was reached by Deguchi et al. (1990) from their analysis of their $J = 1$–0 data and previously published higher-J CO spectra. If the $J = 1$–0 line has an optical depth near unity, the observed emission is sensitive to both the CO column density and the $J = 1$–0 excitation temperature. For this line, the excitation is expected to be mainly by collisions, since the stellar and nebular emission at 4.6 μm is inadequate to produce significant vibrational excitation of CO (see Deguchi et al. 1990). Both Deguchi et al. and Jaminet et al. (1990) infer an average mass-loss rate of $3 \times 10^{-4}\ M_\odot\ \mathrm{yr}^{-1}$ for the molecular envelope, which implies a particle density of $\sim 2 \times 10^4\ \mathrm{cm}^{-3}$ at a radius of 10″ or 1.4×10^{17} cm. This density is close to the critical density for the CO $J = 1$–0 line ($\sim 4 \times 10^4\ \mathrm{cm}^{-3}$), so we expect that T_{ex} is close to the gas kinetic temperature at $R = 10''$. At $R = 30''$, close to the maximum extent of detectable CO $J = 1$–0 emission, the mean gas density is $\sim 2 \times 10^3\ \mathrm{cm}^{-3}$, which is well below the critical density. At this radius, we expect the CO $J = 1$–0 excitation temperature to be below the gas temperature. Deguchi et al. (1990) have solved the equation of thermal balance as a function of radius for the molecular envelope of NGC 7027, including the effects of heating by the central star. They conclude that the gas temperature is not very sensitive to the mass loss rate and has a value of 28 ± 3 K at a radius of 1.2×10^{17} cm (10″). Jaminet et al. (1990) obtain a similar value, 32 ± 5 K at 8″ to fit their observations. The observed average $J = 1$–0 brightness temperature is ~ 12 K for $R = 8''$. If $T_{ex} \approx T_{kin}$, the $J = 1$–0 optical depth must be ~ 0.5, consistent with the claim that the $J = 1$–0 line is not very optically thick even in the inner envelope.

4.2. *Morphology of the Netural Envelope*

The CO $J = 1$–0 brightness temperature distribution shown in Figures 9 and 10 for the central 4 km s^{-1} wide velocity range has a central minimum which coincides with the ionized nebula. Around this minimum is a ring of relatively high brightness temperature. This inner bright ring corresponds to a region of high-density gas adjacent to the ionized nebula. The neutral gas may be heated by a combination of effects including radiative heating of dust grains by the central star and the ionized nebula, and compression by a shock driven by the expansion of the ionized gas (see Kahn 1983; Kwok & Volk 1985; Deguchi et al. 1990). Given the apparent youth of the ionized nebula (~ 2000 yr to reach a radius of 8″ at ~ 17 km s^{-1} expansion velocity) the outer envelope ($r > 20''$) should be essentially undisturbed by the formation of the ionized nebula. If so this outer zone provides direct information on the symmetry and homogeneity of the mass loss by the progenitor star immediately before it revealed itself as the planetary nebula nucleus.

Since, as discussed above, the CO $J = 1$–0 line is not optically thick, the observed morphology of the $J = 1$–0 line probably indicates a non-spherical axisymmetric density distribution in the molecular gas. Such a distribution could result either from (1) an enhanced mass loss in the equatorial plane (i.e., orthogonal to the P.A. 150° symmetry axis); or (2) from a higher wind velocity along the pole than in the equatorial plane; or (3) a combination of (1) and (2). Our $J = 1$–0 data alone are not sufficient to decide which possibility is most likely. Masson et al. (1985) and Jaminet et al. (1990) have noted the presence of emission in high-velocity wings in the $J = 2$–1 and 3–2 spectra which are weak in the 1–0 line, and which suggest the presence of a bipolar outflow component in the neutral envelope. This outflow may be driven by the pressure of the ionized gas near the star. Jaminet et al. argue that the mass loss is substantially nonspherical, with a higher rate in the equatorial plane. If so, the observed $J = 1$–0 morphology is determined both by the mass-loss rate per unit surface area of the progenitor star, and by the velocity field of the expanding envelope.

Despite the apparent overall symmetry, the CO images in Figures 5 and 9 also show small-scale irregularities in the brightness distribution. These are most prominent as alternating bright spots and gaps in the inner bright ring at $\sim 10''$ radius, as seen in Figure 9. There are other distinct bright spots in the outer envelope, such as that in Figure 9 at 24″E, 9″S of the center. We believe that these features are real and probably trace local density enhancements. Alternatively, the bright spots could be regions of higher than average $J = 1$–0 excitation temperature within a uniform, $1/r^2$ density envelope. This alternative seems unlikely, however, since there is no obvious reason why the CO excitation should show local enhancements even if the density does not. We therefore favor an explanation for the bright spots in terms of spatially or temporally nonuniform mass loss from the progenitor star. In this interpretation these CO $J = 1$–0 bright spots would be clumps of higher than average density in the precursor AGB star envelope.

Although models for the CO emission from evolved star envelopes typically assume a spherically symmetric $1/r^2$ distribution (e.g., Knapp & Morris 1985), there is certainly evidence for small-scale clumping in the envelopes of related objects. For example, high-resolution maps of OH and SiO masers in the envelopes of Mira variables, cool supergiants, and OH/IR stars show evidence for clumpy, anisotropic mass loss (Bowers, Johnston, & de Vegt 1989; McIntosh et al. 1989; Alcock & Ross 1986a, b). If such objects are similar to the precursor star of NGC 7027, it is not surprising that the CO distribution we observe also shows indications of density clumps in the extended molecular envelope around the planetary nebula.

4.3. *Relationship between Ionized Nebula and Neutral Envelope*

The ionized component of NGC 7027 has been imaged over a wide range of wavelengths, including visible (e.g., Atherton et al. 1979), near IR (Bentley 1982; Woodward et al. 1990), and radio continuum (Scott 1972; Basart & Daub 1982; Masson 1986, 1989). Atherton et al. find that there is significant differential extinction, amounting to a variation of more than a magnitude in the visual across the nebula. The 4.89 GHz radio continuum image of Masson (1989) is, of course, unaffected by extinction and has an angular resolution of 1″.05, so should give an excellent representation of the distribution of the ionized gas. In Figure 11, we present contours of Masson's (1989) 4.89 GHz continuum map, shown as dotted contours overlaid on contours of the inner portion of the CO $J = 1$–0 distribution for the central velocity range (Fig. 9) shown as solid contours. Despite the factor of 5 difference in angular resolution, there is a striking correlation between the two images. The ionized gas fits neatly into the central minimum of the CO distribution. The two bright peaks of the radio continuum map lie just inside and are collinear with, the two main CO emission peaks. The weak "horns" or ansae, extending NW and SE in the continuum map appear to point toward the

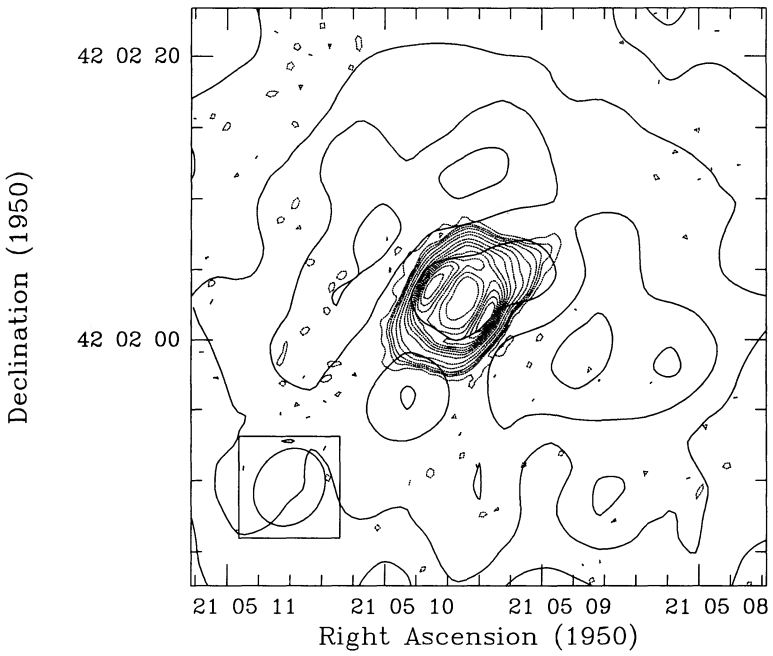

FIG. 11.—Comparison of the location of molecular and ionized gas in NGC 7027. The heavier contours are the CO intensity from Fig. 9 (showing the envelope in cross section), replotted with a contour interval of 1.0 Jy per clean beam for clarity. The lighter contours, closely spaced at the center, are from the 4.89 GHz VLA map of Masson (1989), plotted at levels of 0.1, 0.2, 0.5, 1, 2, 5, 10, 20, ..., 90% of the continuum maximum of 0.170 Jy beam^{-1}. Clean beam for the continuum map was 1".05 FWHM. Note the correspondence between features in the two sets of data.

gaps in the inner bright ring of CO emission. This effect is especially noticeable to the NW but is also evident on the SE side of the ionized distribution, where the radio continuum contours seem to bulge around the bright CO peak at R.A. $21^h05^m09^s.85$, Decl. 42°01'56" (equinox 1950).

In comparing these two images, it is important to keep in mind that the CO distribution in Figure 11 is of the central velocity range only, and so gives a cross-sectional view, with intensity approximately proportional to molecular column density (provided $\tau \lesssim 1$, as we have argued is the case). In contrast, the radio continuum is proportional to the emission measure integrated over all velocities in the ionized gas. Various authors have modeled the ionized gas distribution as a hollow cylinder (e.g., Scott 1973; Bentley 1982) or prolate spheroid (Atherton et al. 1979; Masson 1989). The correspondence in morphology between the CO and ionized gas distributions strongly suggests a causal connection between the two. It has been argued that the overall structure of the ionized gas may reflect the interaction between the photoionized AGB star envelope and a fast, hot wind from the central star (see Dopita & Meatheringham 1990; Kwok & Volk 1985). The bright peaks in the radio continuum along the minor axis of the nebula indicate a higher electron density in the equatorial plane than along the polar axis (at P.A. 150°). Since the CO distribution also shows higher brightness temperatures—presumably due to a larger CO column density—in the minor axis, the higher emission measure of the ionized gas is evidently a result of photoionization of the denser parts of the precursor neutral wind. The dimension at P.A. 60° is smaller than at 150° because the higher density retards the expansion of the ionized nebula in the equatorial plane relative to the lower density polar direction. The overall morphology of the ionized gas, then, is probably determined mainly by the density distribution of the molecular wind from the precursor AGB star, rather than by the ram pressure of a fast ionized stellar wind from the planetary nebula nucleus.

The ansae in the ionzed gas (cf. Masson 1989 and Fig. 11) appear to coincide with gaps in the inner bright ring of CO emission. Since the pressure of the ionized gas is extremely high, with $T_e = 14,000$ K (Basart & Daub 1987) and $n_e \approx 10^5$ cm^{-3} (Atherton et al. 1979, but adopting a distance of 0.9 kpc), the ionized region should tend to expand more rapidly into lower density regions of the neutral material. The NW projection of the radio continuum between the main CO peaks is probably a result of this effect. The bulging of the continuum contours to the SE may also indicate expansion into a lower density region leading eventually to more pronounced ansae there as well.

4.4. *Comparison with Other CO Observations of Planetary Nebulae*

Other planetary nebulae which have been mapped in CO emission include NGC 6720 (the "Ring" Nebula), NGC 2346, and IRAS 21282+5050. These objects resemble NGC 7027 in their molecular properties, but with significant differences. Bachiller et al. (1989a, b) and Healy & Huggins (1988) find that both NGC 6720 and NGC 2346 have CO emission in a clumpy, ringlike distribution surrounding the central star. These molecular envelopes closely match the size of the optical emission from the ionized gas, in contrast to NGC 7027 where the CO distribution is clearly exterior to and much larger than the ionized nebula. The CO in NGC 6720 and NGC 2346 is much less regular than in NGC 7027, and the line profiles

indicate velocities in the CO which are disturbed compared with the apparently regular expansion of NGC 7027.

The CO $J = 2$–1 excitation temperature inferred for NGC 6720 is 16–38 K (Bachiller et al. 1989a), a range quite similar to that for NGC 7027. However, the molecular mass in both NGC 6720 and NGC 2346 is very much less than for NGC 7027—0.1 $M_\odot$ for the former two, but $\sim 3\ M_\odot$ for NGC 7027 (Jaminet et al. 1991). These differences suggest that NGC 6720 and NGC 2346 are in a more advanced evolutionary state than NGC 7027, so that the effects of the central star, by photodissociation of CO and possibly by a fast ionized wind, acting on the precursor molecular envelope, have had a greater effect.

IRAS 21282+5050, in contrast, seems to be at a less-developed evolutionary stage. Although its distance is uncertain, a value of 2 kpc is likely (Likkel et al. 1988; Shibata et al. 1989), or about twice that of NGC 7027. Yet its 115 GHz continuum flux density is at least 100 times weaker than NGC 7027 (Shibata et al. 1989), implying a free-free luminosity at least 25 times weaker. Evidently the ionization of the circumstellar material is less advanced in IRAS 21282 than in NGC 7027. Even so, both objects show CO emission which is clumpy, not smooth, so clumpiness is intrinsic to the mass loss from the precursor stars.

In trying to establish the relative evolutionary status of planetary nebulae based on the properties of the neutral wind and ionized gas, it is important to bear in mind that the progenitor stars may have different intrinsic properties (especially initial mass) and mass loss histories. NGC 7027 has a mass-loss rate of $\sim 3 \times 10^{-4}\ M_\odot\ \mathrm{yr}^{-1}$ just prior to onset of planetary nebula formation (Jaminet et al. 1991), while IRAS 21282, if at a distance of 2 kpc, may have a rate of $\sim 6 \times 10^{-5}\ M_\odot$, a factor of 5 lower (Likkel et al. 1988). The density and total mass of the molecular envelope must have a strong influence on the evolution of the planetary nebula (as we have argued above). The differences in evolutionary status for these objects may be as much a conseqence of differences in the initial state of the neutral envelope as of the length of time since the central star began ionizing the surrounding gas.

5. SUMMARY

We have mapped the CO $J = 1$–0 emission toward the young planetary nebula NGC 7027 by combining interferometer and single-dish observations. The resulting images have angular resolution of 4".8 × 5".7 and velocity resolution of 1 km s^{-1} and contain all the flux in the CO line. The images show that the CO distribution has a large-scale axial symmetry which is aligned with the symmetry axis of the ionized gas. We also find, however, that the molecular gas has several bright spots of CO emission. Since the $J = 1$–0 line has an optical depth near unity, these bright spots are probably local density enhancements which may have resulted from nonuniform mass loss by the precursor AGB star. The morphology of the bright inner CO emission matches the distribution of the ionized gas: the main peaks in both the ionized continuum emission and the CO $J = 1$–0 line are adjacent and collinear. The "ansae" in the ionized gas appear to be projecting toward or through gaps in the CO distribution. We interpret this correspondence between ionized and molecular features as evidence that the density distribution of the ionized gas is determined mainly by the gas density of the precursor AGB star envelope. The radial dependence of the ionized density may result from ram pressure of a fast stellar wind on the ionized envelope. However, the dependence on polar angle is determined by the molecular envelope density, which in turn depends on the angular distribution of mass loss from the precursor star. The ionized ansae associated with gaps in the bright inner CO ring may be pressure instabilities where the expanding ionized gas is forcing its way into regions of lower than average density in the molecular gas. The morphology and evolution of the ionized nebula appear to be controlled by the density distribution of the neutral envelope.

We thank Colin Masson for providing his VLA images in digital form . Reasearch at the University of California, Berkeley, Radio Astronomy Laboratory is supported in part by NSF grant AST 87-14721.

REFERENCES

Alcock, C., & Ross, R. 1986a, ApJ, 305, 837
———. 1988b, ApJ, 310, 838
Atherton, P. D., Hicks, T. R., Reay, N. K., Robinson, G. J., Worswick, S. P., & Phillips, J. P. 1979, ApJ, 232, 786
Bachiller, R., Bujarrabal, V., Martin-Pintado, J., & Gomez-Gonzalez, J. 1989a, A&A, 218, 252
Bachiller, R., Planesas, P., Martin-Pintado, J., Bujarrabal, V., & Tafalla, M. 1989b, A&A, 210, 366
Basart, J. P., & Daub, C. T. 1987, ApJ, 317, 142
Bentley, A. F. 1982, AJ, 87, 1810
Bowers, P. F., Johnston, L. J., & de Vegt, C. 1989, ApJ, 340, 479
Deguchi, S., Izumiura, H., Kaifu, N., Mao, X., Nguyen-Q.-Rieu, & Ukita, N. 1990, ApJ, 351, 522
Dopita, M. A., & Meatheringham, S. J. 1990, ApJ, 357, 140
Healy, A. P., & Huggins, P. J. 1988, AJ, 95, 866
Huggins, P. J., & Healy, A. P. 1989, ApJ, 346, 201
Jaminet, P. A., Danchi, W. C., Sutton, E. C., Russell, A. P. G., Sandell, G., Bieging, J. H., & Wilner, D. A. 1991, ApJ, submitted
Kahn, F. 1983, in IAU Symp. 103, Planetary Nebulae, ed. D. R. Flower (Dordrecht: Reidel), 305
Knapp, G. R., & Morris, M. 1985, ApJ, 292, 464
Kutner, M. L., & Ulich, B. L. 1981, ApJ, 250, 341
Kwok, S., & Volk, K. 1985, ApJ, 299, 191
Likkel, L., Forveille, T., Omont, A., & Morris, M. 1988, A&A, 198, L1
Masson, C. R. 1986, ApJ, 302, L27
———. 1989, ApJ, 336, 294
Masson, C. R., et al. 1985, ApJ, 292, 464
McIntosh, G. C., Predmore, C. R., Moran, J. M., Greenhill, L. J., Rogers, A. E. E., & Barvainis, R. 1989, ApJ., 337, 934
Menessier, M. O., & Omont, A., eds. 1990, From Miras to Planetary Nebulae: Which Path for Stellar Evolution? (Gif sur Yvette: Editions Frontieres)
Mufson, S. L., Lyon, J., & Marionni, P. A. 1975, ApJ, 291, L85
Morris, M. 1975, ApJ, 197,603
Phillips, J. P., White, G. J., & Richardson, K. J. 1985, A&A, 151, 421
Scott, P. F. 1973, MNRAS, 161, 35p
Shibata, K. M., Tamura, S., Deguchi, S., Hirano, N., Kameya, O., & Kasuga, T. 1989, ApJ, 345, L55
Thronson, H. A. 1983, ApJ, 264, 599
Thronson, H. A., & Bally, J. 1986, ApJ, 300, 749
Ulich, B. 1981, AJ, 86, 1619
Ulich, B., & Haas, R. 1976, ApJ, 30, 247
Urry, W. L., Thornton, D. D., & Hudson, J. A. 1985, PASP, 97, 745
Vogel, S. N., Wright, M. C. H., Plambeck, R. L., & Welch, W. J. 1984, ApJ, 283, 655
Weliachew, L., Emerson, D. T., Forveille, T., Bieging, J. H., Wright, M. C. H., & Ellder, J. 1985, A&A, 153, 139
Woodward, C., Pipher, J. L., Shure, M., Forrest, W. J., & Sellgren, K. 1990, ApJ, 342, 860